Available online at www.sciencedirect.com

SciVerse ScienceDirect

Ceramics International 39 (2013) 5093–5102

CERAMICS INTERNATIONAL

www.elsevier.com/locate/ceramint

Sintering of electron beam physical vapor deposited thermal barrier coatings under flame shock

Chen Chen[a,b,c], Hongbo Guo[b], Shengkai Gong[b,*], Xiaofeng Zhao[c], Ping Xiao[c,*]

[a]AVIC Commercial Aircraft Engine CO. LTD., Shanghai 200241, China
[b]School of Materials Science and Engineering, Beihang University, Beijing 100191, China
[c]School of Materials, University of Manchester, M13 9PL, UK

Received 1 November 2012; received in revised form 14 November 2012; accepted 2 December 2012
Available online 4 January 2013

Abstract

Flame shock treatment of electron beam physical vapor deposited (EB-PVD) thermal barrier coatings (TBCs) was carried out to investigate the degradation of TBCs exposed to a temperature gradient. The flame treatment resulted in temperature gradients both in the surface plane and through the thickness of the TBCs. TBC densification occurred where the flame was centered and resulted in a fine crack network at the surface of the TBC. The TBCs with addition of 0.5 wt% alumina were made, in which alumina was used as stress sensors for stress measurements by photoluminescence piezo-spectroscopy (PLPS). This allowed stress measurements to be made through the TBC thickness using a depth sensing method. Such stress measurements help us to better understand the densification of the TBCs.

Keywords: Thermal barrier coatings; Photoluminescence piezo-spectroscopy; Sintering; Flame shock

1. Introduction

Thermal barrier coatings (TBCs) are widely used in gas turbines for both propulsion and power generation [1–3]. The development of electron beam physical vapor deposited (EB-PVD) TBCs mainly aims at improving the durability during thermal cyclings compared to plasma sprayed TBCs [4]. Sintering of TBCs during service at high temperature is undesirable, since it would reduce the thermal shock resistance and cause degradation of thermal barrier performance as a result of the increased thermal conductivity [5].

The as-deposited EB-PVD TBCs have a columnar structure with individual columns having a feather-like structure. Thermal exposure of EB-PVD TBC would cause bridging between feather-arms within the columns, but inter-column connection requires a relatively long duration [5]. The build-up of tensile stress within the top layer can be sufficiently large to lead to mud-cracking due to inter-columnar sintering [3]. Mud-cracking relieves the in-plane tensile stress within the clusters, and thereby accelerates the inter-columnar sintering within each cluster [6].

Considering studies carried out in a uniform temperature field, the sintering behavior of the coating should be uniform. However, non-uniform temperature field occurred very often in the real circumstances. The thermal gradient will result in a different stress distribution. Zhang et al. studied the effect of thermal shock on TBCs using four concave mirrors to focus infrared light on a narrow area to achieve high temperature and fast heating. It was reported that the maximum stress occurred with the highest temperature gradient. However, only a few studies concerned sintering behavior in a temperature gradient [7,8]. In this work, flame shock was employed to create temperature gradients both in the TBC surface and through the TBC thickness direction as well, to simulate the service environment of gas turbine engines [9]. Previous research showed that the failure behavior of TBCs during

*Corresponding authors.
E-mail addresses: gongsk@mse.buaa.edu.cn (S. Gong), ping.xiao@manchester.ac.uk (P. Xiao).

0272-8842/$ - see front matter © 2013 Published by Elsevier Ltd and Techna Group S.r.l.
http://dx.doi.org/10.1016/j.ceramint.2012.12.005

flame shock was different from that during the isothermal heat treatment [10]. Flame shock resulted in a temperature gradient in both in-plane (parallel to the interface) and out-of-plane (through-thickness) directions. This temperature gradient was expected to result in a variation in sintering behavior with positions. As Young's modulus of TBCs increased due to sintering [11,12], the temperature gradient obviously resulted in a variation in Young′s modulus.

In order to further understand the sintering behavior of TBCs during flame shock, the residual stress of TBC layer through the thickness direction was studied. Although some engineering methods have already been widely used in various kinds of TBCs, such as X-ray diffraction [13,14], neutron diffraction [14,15], curvature measurement [16,17] and substrate removal with the strain measurement technique [17,18], it is still hard to measure the local residual stress using these techniques [17]. As a promising potential non-destructive evaluation (NDE) method, photoluminescence piezo-spectroscopy (PLPS) has been explored to study the failure mechanism of TBC systems by assessing the residual stress levels in the thermally grown oxide (TGO) [19–21]. PLPS was based on the stress dependant R-line fluorescence resulting from the persistent Cr^{3+} impurity in alumina [22]. This method used embedded alumina in the coating as a stress sensor to obtain the residual stress in the TBCs. In particular, the residual stress gradient of TBC along thickness direction could also be analyzed.

The residual stress in embedded particles includes two components, known as the microstress and the macrostress. The microstress refers to the residual stress caused by thermal mismatch between embedded alumina and surrounding YSZ coating matrix, while macrostress refers to the residual stress induced by the thermal mismatch between the metallic substrate and the ceramic coating. The evolution of the macrostress is induced by the growth of TGO and creep of the bond coat and TGO. Changes in microstress are caused mainly by the degradation of YSZ coating matrix, in particularly Young′s modulus.

In order to utilize alumina in TBC as a PLPS stress sensor, in previous work it has been reported that YSZ TBC was impregnated by an alumina precursor (alumina nitride), followed by heat treatment [23]. However, it has been contested that alumina might not be fully embedded in the YSZ matrix. In this experiment, alumina was embedded in YSZ top coat during the deposition procedure using EB-PVD.

In this work, the sintering behavior of EB-PVD TBC under flame shock was investigated using PLPS accompanied by microstructural analysis. In particular, the residual stress measurement in the through-thickness direction was used to investigate the sintering behavior across the TBC thickness. By quantification of the microstress measured by PLPS the distribution of TBC′s Young′s modulus along the TBC thickness direction was also characterized.

2. Experimental details

2.1. Sample preparation

The samples used in this study were prepared by EB-PVD, with Nickel-based super alloys as the substrate, NiCoCrAlY as the bond coat, and 8 mol% Y_2O_3 stabilized ZrO_2 (8YSZ) as the top coat. The details of materials in each layer are shown in Table 1. In order to obtain fluorescence signals from the top coat, 0.5 wt% Al_2O_3 doped YSZ targets were used for preparing alumina embedded YSZ ceramic coating. The thickness of the top coat and the bond coat was ~120 μm and ~50 μm, respectively. The deposited samples were heat treated at 700 °C for 2 h and then at 1000 °C for 2 h.

2.2. Flame shock experiment

The flame shock testing system consisted of a high temperature gas with high velocity heating the TBC surface and compressed air cooling at the substrate. The surface temperature of the top coat was measured by infrared detector, while the substrate temperature was measured by thermocouple.

The samples were 32 mm in diameter, while the flame was controlled to be 15 mm in diameter and concentrated on the TBC surface. The schematic of the samples under the flame test is illustrated in Fig. 1.

Table 1
Nominal composition of substrate super alloy.

Element content (wt%)								
Substrate								
Ni	Cr	Co	W	Mo	Al	Ti	Ta	Hf
Balance	9.0	10.0	7.0	2.0	5.1	0.9	3.8	1.5
Bond coat								
Ni	Co	Cr	Al	Y				
Balance	10.34	23.66	8.56	0.91				

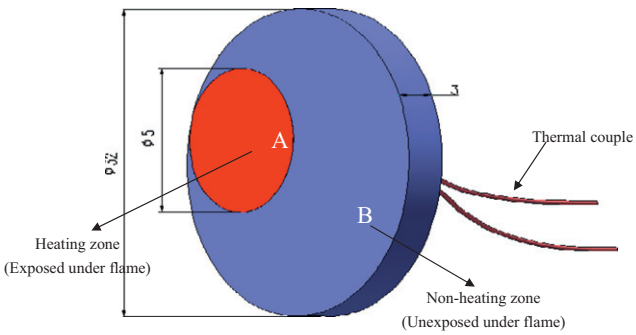

Fig. 1. Schematic of the samples in the flame shock experiment. Region A is the hottest area exposed to flame, while region B is the non-heating zone.

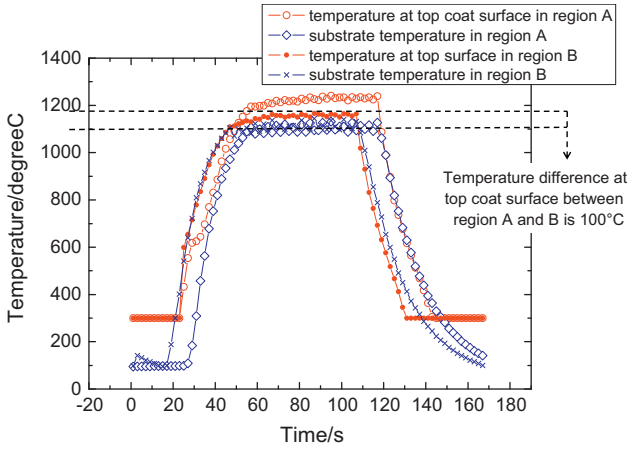

Fig. 2. Temperature profile of the surface of the ceramic coating under flame shock at regions A and B (shown in Fig. 1) of the samples. The temperature difference between two regions is illustrated in the profile.

The substrate temperature was controlled at either 900 °C or 1100 °C by controlling the compressed air velocity. In one circumstance, 300 cycles were carried out with a substrate temperature of ~900 °C. In another, 100 cycles were carried out with a substrate temperature of ~1000 °C. Each cycle consisted of 20 s of heating, 60 s of dwelling and 40 s of cooling. The temperature difference between the substrate and the surface of the top coat in the heating zone was around 200 °C as shown in Fig. 2. The top coat surface temperatures varied with positions as shown for regions A and B in Fig. 2.

2.3. Residual stress measurement using PLPS

After the flame shock treatment the stress at different positions on the sample surface was measured using PLPS. In this experiment, fluorescence was stimulated by a He–Ne laser (632.78 nm wavelength, Horiba JY-HR800, France) focusing onto the sample using an optical lens (50 ×, 0.55 numerical aperture, Olympus). The theoretical resolution of the detecting diameter was less than 1 μm. The fluoresced light was passed through a diffraction grating and detected by a CCD.

R-line peak doublets of R_1 and R_2 were deconvoluted by a commercial Renishaw Wire software. Sapphire and alumina powders, which were treated as zero stress samples, were measured at 14,402 and 14,432 cm^{-1} for the peak positions of R_1 and R_2, respectively. Accordingly, the shift of R_2 peak from the zero stress sample was obtained [24,25]. Then residual stresses could be obtained according to [26]:

$$\Delta\bar{\nu} = \Pi\bar{\sigma} \tag{1}$$

where $\bar{\sigma}$ is the stress in alumina, Π is the piezo-spectroscopic tensor ($\Pi = 7.60\ cm^{-1}$/GPa for polycrystalline α-alumina under hydrostatic loading) and $\Delta\bar{\nu}$ is the measured PLPS shift from the zero stress peak position.

Through-thickness analysis was also employed in this investigation. A peak shift profile was obtained by moving focal point of the laser from surface of the coating towards the interface with the bond coat. In this study, the value of peak position at the surface of the TBC was set as zero. Hence the peak shift in relation to that at the TBC surface indicated whether the stress was in compressive or tensile relative to the TBC surface stress. To identify the penetration depth of the laser, an EB-PVD TBC produced using the same processing procedure without alumina addition was taper-polished. PLPS was used on this sample to measure the TGO signal that penetrated through the TBC at various thicknesses. The penetration depth of the PLPS measurement through the TBC was 32 μm.

2.4. Finite element analysis

The Finite Element (FE) analysis was performed using the ANSYS 9.0 software (ANSYS Inc., Canonsburgh, PA, USA) to simulate the temperature profile and the stress profile in TBCs.

The specimen structure was composed of three layers: super alloy substrate (3 mm), bond coat (0.05 mm) and top coat (0.1 mm). The 2D coupled-field solid element PLANE13 was selected. In the simulation, the distance from the heating center of zone A in Fig. 1 to the far end of zone B in Fig. 1 was 24.5 mm. In the simulation model, the heating radius was 7.5 mm, while the non-heating length was 17 mm. The model was meshed using quadrilateral-shaped elements. In this simulation, symmetric boundary conditions were used.

The following assumptions and boundary conditions were used:

(1) all layers were homogeneous and isotropic,
(2) all layers were initially stress-free at deposition temperature (800 °C),
(3) side surface was thermal insulation; the creep and plastic deformation of all layers were negligible and were not taken into account, and
(4) three-dimensional problem was reduced to a two-dimensional one.

In the simulation, thermal-elastic constitutive equations were employed from the ANSYS help file:

$$\{\varepsilon\} = [D]^{-1}\{\sigma\} + \{\alpha\}\Delta T \tag{2}$$

$$S = \{\alpha\}^T\{\sigma\} + \frac{\rho C_p}{T_0}\Delta T \tag{3}$$

where, $\{\varepsilon\} = [\varepsilon_x \varepsilon_y \varepsilon_z \varepsilon_{xy} \varepsilon_{yz} \varepsilon_{xz}]^T$ is total strain vector, S is entropy density,

$$[D]^{-1}=\begin{bmatrix} \frac{1}{E_x} & \frac{-v_{xy}}{E_x} & \frac{-v_{xz}}{E_x} & 0 & 0 & 0 \\ \frac{-v_{yx}}{E_y} & \frac{1}{E_y} & \frac{-v_{yz}}{E_y} & 0 & 0 & 0 \\ \frac{-v_{zx}}{E_z} & \frac{-v_{zy}}{E_z} & \frac{1}{E_z} & 0 & 0 & 0 \\ 0 & 0 & 0 & \frac{1}{G_{xy}} & 0 & 0 \\ 0 & 0 & 0 & 0 & \frac{1}{G_{yz}} & 0 \\ 0 & 0 & 0 & 0 & 0 & \frac{1}{G_{zx}} \end{bmatrix}$$

= elastic stiffness matrix,

$\{\sigma\}=[\sigma_x\sigma_y\sigma_z\sigma_{xy}\sigma_{yz}\sigma_{xz}]^T$ is stress vector, T_0 is absolute reference temperature, T is current temperature, T_{ref} is reference temperature, ΔT is $T-T_{ref}$, ρ is density and C_p is specific heat at constant stress or pressure.

Using $\{\varepsilon\}$ and ΔT as independent variables, and replacing the entropy density S in Eq. (1) by heat density Q using the second law of thermodynamics for a reversible change

$$Q=T_0S$$

we obtain $\{\sigma\}=[D]\{\varepsilon\}-\{\beta\}\Delta T$ and $Q=T_0\{\beta\}^T\{\varepsilon\}+\rho C_v\Delta T$ where $\{\beta\}=[D]\{\alpha\}$ is vector of thermoelastic coefficients and $C_v=C_p-\frac{T_0}{\rho}\{\alpha\}^T\{\beta\}$ is specific heat at constant strain or volume.

Applying the variational principle to stress equation of motion and the heat flow conservation equation coupled by the thermoelastic constitutive equations, produces the following finite element matrix equation:

$$\begin{bmatrix}[M] & [0]\\ [0] & [0]\end{bmatrix}\begin{Bmatrix}\{\ddot{u}\}\\ \{\ddot{T}\}\end{Bmatrix}+\begin{bmatrix}[0] & [0]\\ [C^{tu}] & [C^t]\end{bmatrix}\begin{Bmatrix}\{\dot{u}\}\\ \{\dot{T}\}\end{Bmatrix}+\begin{bmatrix}[K] & [K^{ut}]\\ [0] & [K^t]\end{bmatrix}\begin{Bmatrix}\{u\}\\ \{T\}\end{Bmatrix}=\begin{Bmatrix}\{F\}\\ \{Q\}\end{Bmatrix}$$

where $[K]$ is element stiffness matrix, $[M]$ is element mass matrix, $\{F\}$ is sum of element nodal force and element pressure vectors, $[K^t]$ is element diffusion conductivity matrix, $[C^t]$ is element specific heat matrix, $\{Q\}$ is sum of the element heat generation load and element convection surface heat flow vectors, $[K^{ut}]$ is element thermoelastic stiffness matrix $=-\int_{vol}[B]^T\{\beta\}(\nabla\{N\}^T)d(vol)$, $[B]$ is strain displacement matrix based on the element shape functions $\{N\}$, and $[C^{tu}]=-T_0[K^{ut}]^T$ is element thermoelastic damping matrix. Parameters of all layers used in the simulation are listed in Tables 2–4.

3. Results

3.1. Surface morphology and microstructure

After flame shock testing, different positions of the TBC surface were examined by optical microscope. It was found that the crack density of the top coat changed gradually with position away from the flame center. Images were taken at the center of region A labeled in Fig. 1, and at 7, 14 and 21 mm away from the center (Fig. 3).

Using a SISC–IAS image analysis software developed by KYKY Technology Development Ltd., the mean size of cracked area was obtained, which is illustrated in Table 5. Thus, the crack density can be quantified.

Fig. 3 shows that within the heating area the cracks were denser and coarser than those in the other areas. Crack density also decreased with the increased distance away from the heated area. Crack density was thought to be related to the volume shrinkage due to sintering which varied with the temperature gradient. The temperature

Table 2
Parameters for superalloy.

T·(K)	293	473	573	673	773	873	973	1073	1173	1273	1373
λ·(Wimp^{-1} K^{-1})		9.67	11.47	13.44	14.99	16.79	17.96	19.63	19.51	19.43	19.00
c (J/kg K)		385	427	456	481	498	506	506	489	473	443
α (10^{-6} K^{-1})			12.36	12.91	13.15	13.41	13.98	14.49	15.01	15.93	16.94
E (GPa)	127.6	124.0	121.0	118.0	114.0	110.0	105.0	100.0	93.5	84.0	
v	0.33		0.33		0.34	0.34	0.36	0.36	0.37	0.38	

T is temperature; λ is thermal conductivity; α is coefficient of thermal expansion; E is elastic Young's modulus; and v is Poison's ratio.

Table 3
Parameters for NiCoCrAlY bond coat [27]. Symbols are as for Table 2.

T·(K)	293	473	673	873	1073	1273	1373
λ (Wimp^{-1} K^{-1})	5.8	7.5	9.5	12.0	14.5	16.2	17.0
α (10^{-6} K^{-1})	13.6	14.2	14.6	15.2	16.1	17.2	17.6
E (GPa)	200	190	175	160	145	120	110
v	0.30	0.30	0.31	0.31	0.32	0.33	0.33

Table 4
Parameters for 8YSZ top coat [27]. Symbols are as for Table 2.

T (K)	293	473	673	873	1073	1273	1373
$\lambda \cdot (\mathrm{Wimp}^{-1}\,\mathrm{K}^{-1})$	1.9	1.8	1.7	1.6	1.6	1.7	1.7
α $(10^{-6}\,\mathrm{K}^{-1})$	9.0	10.0	9.7	9.8	10.0	10.3	10.3
E (GPa)	48	47	44	40	34	26	22
v	0.10	0.10	0.10	0.11	0.11	0.12	0.12

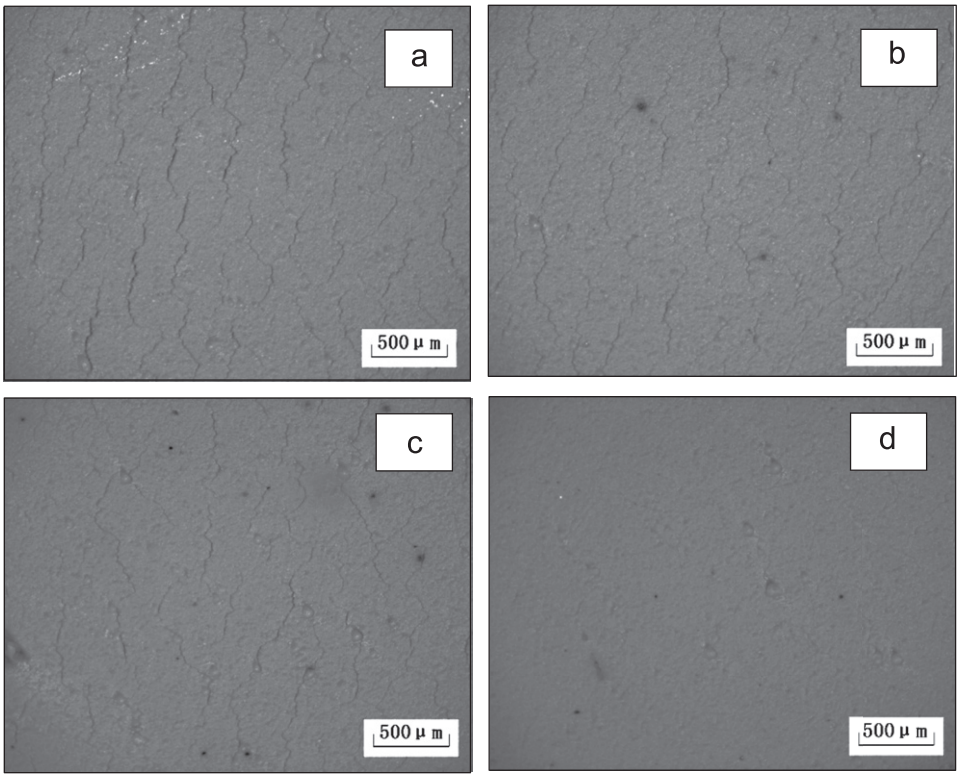

Fig. 3. Surface morphology of the ceramic coating after 300 cycles of flame shock. The substrate temperature was controlled at 900 °C; (a) was taken from the heating center, while (b, c and d) were taken away from the heating center at every 7 mm.

Table 5
Mean size of cracked area.

Position code[a]	a	b	c	d
Mean cracked size/mm[b]	0.24	0.31	0.38	–

[a]Position code was attached to the area label mentioned in Fig. 3.
[b]Mean cracked size denoted the mean length between neighbored cracks. In this investigation, ten analyzing lines were plotted uniformly in each photo. Using the SISC–IAS image analysis software, mean length between neighbored cracks was attained.

difference between the heated zone and the non-heated zone shown in Fig. 2 would be discussed in detail later.

In order to observe the sintering across the temperature gradient, the microstructures of the fracture sections at different depth were studied using SEM. Fig. 4 shows SEM photos taken at both regions A and B (as shown in Fig. 1) after a flame shock test with the substrate temperature controlled at 900 °C. Fig. 4a was taken from the same area as Fig. 3a i.e. region A, while Fig. 4b was taken from the same area as Fig. 3d i.e. region B.

In Fig. 4a, sintering occurred in the ceramic coating, not only in the columns, but also between the columns whereas in Fig. 4b, outside the heated area, little sintering occurred. For comparison, flame treatments for 100 cycles were performed with the substrate temperature controlled at 1100 °C. Fig. 5 shows the fractured TBC cross-section in the heated zone.

Although very short heating duration was performed on this sample (totally 200 min including the heating procedure and temperature dwelling procedure), very severe sintering occurred at the surface of the coating. Compared to the sample treated at a lower temperature and for longer duration (shown in Fig. 4), heavier sintering occurred. This suggested that the temperature dominated the sintering of the ceramic coating rather than heating duration.

It should be noted that this phenomenon was different from that after the isothermal heat treatment. Sintering between columns during isothermal heating requires over

100 h at 1100 °C to occur [4,5,28]. However, in Fig. 5, with the surface temperature of 1250 °C, sintering happened in only 200 min. It implies that sintering at surface of the coating is more severe under the flame treatment than uniform heating by furnace.

3.2. Residual stress measurement using PLPS

Fig. 6 shows the peak shift of PLPS measurements as function of the laser focus position for the TBC after 300 cycles of flame treatment with substrate temperature at 900 °C and surface temperature at 1200 °C. The profile was obtained from at least five samples with the same preparation procedure and flame treatment method. The focal position was changed from the surface into the coating and the peak position was measured relative to the peak position of the spectra focused at the surface of the TBC. With increased penetration depth of the laser beam the peak shift increased, suggesting that the stresses became more tensile with increasing penetration depth, which contradicts with a previous work [29], where stress was found to be more compressive with increased distance from the TBC surface to the TBC/substrate interface. However, this previous work was carried on TBCs treated isothermally. During the short time of the isothermal heat treatment, lower temperature was obtained in ceramic coating compared to which tested under the flame treatment. Hence, slighter

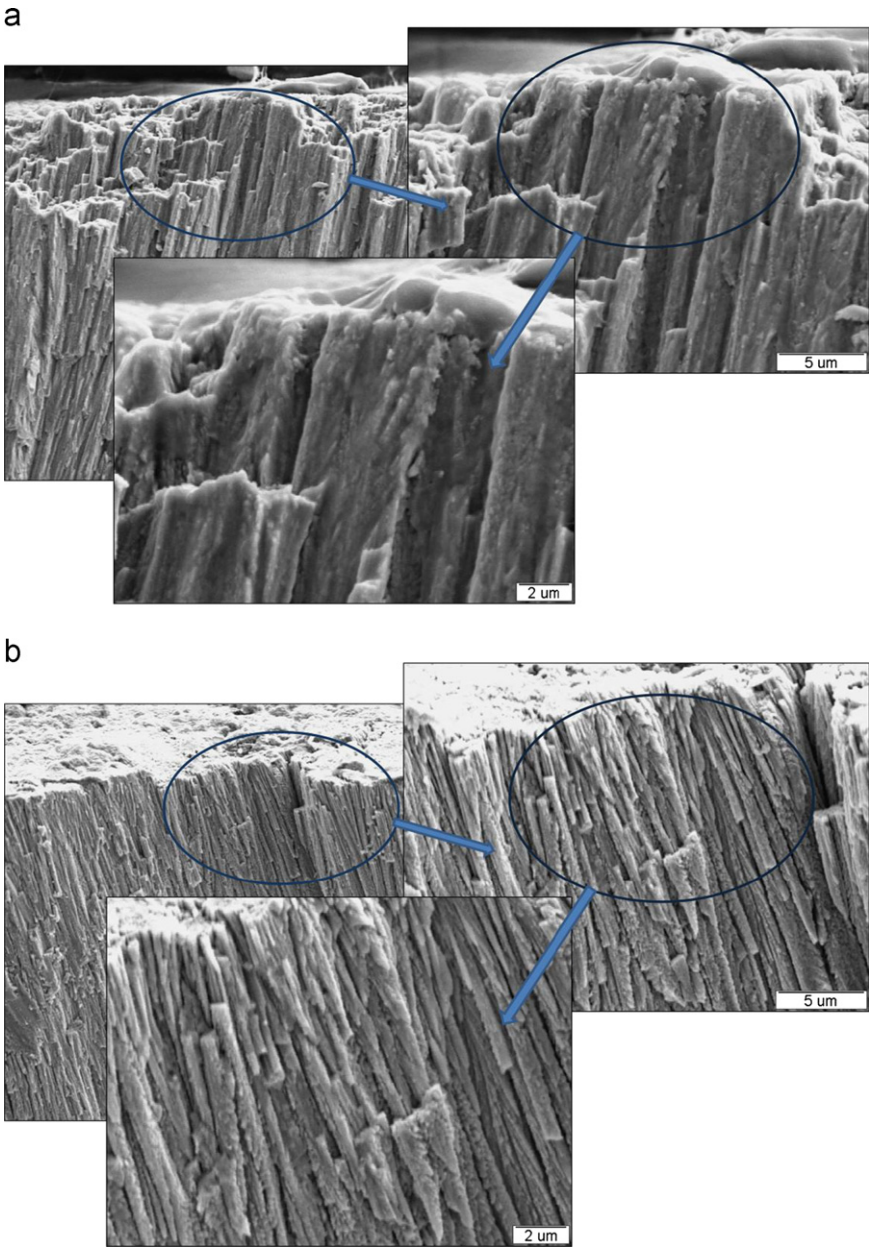

Fig. 4. (a) Fracture section of the top coat at region A (heated area) and (b) fracture section of the top coat at region B (non-heated area). The sample underwent flame shock for 300 cycles. The substrate temperature was controlled at 900 °C, while the highest temperature of the coating surface was measured as 1200 °C.

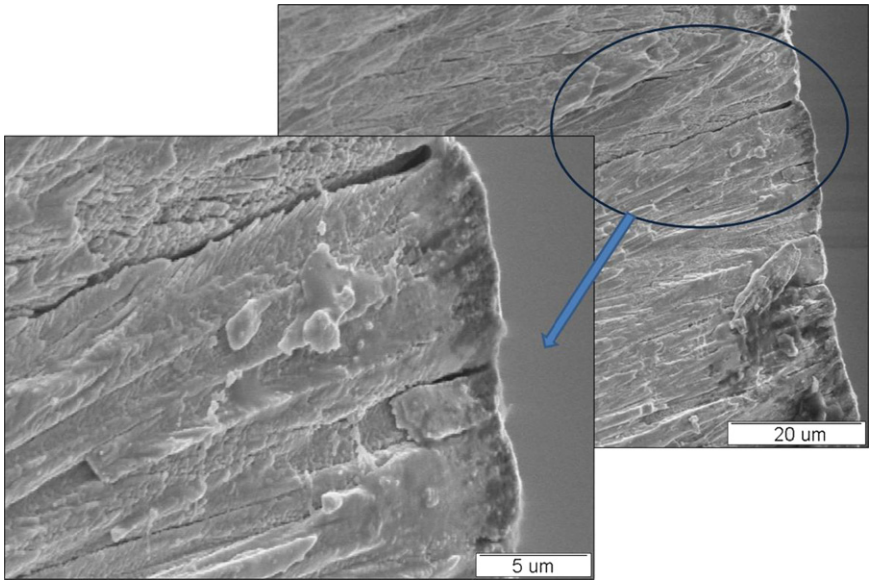

Fig. 5. Fracture section of the top coat surface at region A (heated zone). In this thermal shock experiment, the substrate temperature was controlled at 1100 °C, while the surface of the coating was measured as 1200°C. The sample was tested under flame shock for 100 cycles. It was seen that sintering between columns was heavier than that shown in Fig. 4.

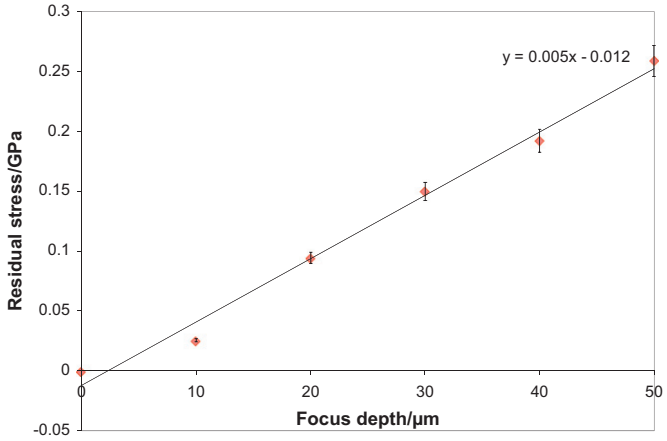

Fig. 6. Stress profile along through the thickness direction of the ceramic coating at the center of heated zone, which suggests that the compressive stress is increasing from TBC surface toward TBC/substrate interface. The samples were tested under flame shock with substrate temperature at 900 °C for 300 cycles. The compressive stress at surface of the sample was 790 MPa, and it was artificially set as zero in the investigation.

sintering occurred in isothermally heat treated coating and the columnar structure was still maintained. Therefore, the residual stress gradient is mainly controlled by the thermal mismatch between the substrate and the ceramic coating. An increased compressive stress profile was shown with the increasing of the focus depth from surface of the coating.

4. Discussion

4.1. Temperature profile

In this experiment the flame was focused on a fixed area (Fig. 1). The temperature profile was simulated using the ANSYS (described in Section 2.4) by assuming region A was uniformly heated and is illustrated in Fig. 7. The temperatures along the surface and through the coating thickness were also plotted in Fig. 7a and b, respectively.

In order to simplify the simulation model, region B was assumed to be heated only by the heat exchange from region A. However, in reality, the flame heating decays gradually away from this heating zone, instead of such change of temperature across A and B shown in the simulation. As a result, the calculated surface temperature difference of 250 °C (Fig. 7b) from the heating zone to the non-heating zone was much more than that of 100 °C from experimental measurements (Fig. 2). Nevertheless, the difference of sintering behavior between the heating zone and the non-heating zone was obvious (see Fig. 4). Meanwhile, the simulated temperature profile across the TBC thickness showed a temperature difference of 100 °C from the TBC surface to the TBC/substrate interface, whereas the temperature control at the surface and the substrate allowed difference of over 200 °C between them. Cooling at the back side of the substrate may increase the temperature difference between the substrate back surface and the top surface of TBCs during flame treatment experiments.

4.2. Surface crack formation

After flame treatments, mud crack phenomena were observed and these might be caused by tensile stresses generated during the flame treatment. The highest tensile stress should occur during fast heating. It is impossible to measure such stresses during the flame treatment with our current facility, so the stress profile is simulated using the ANSYS software. Fig. 8 shows the in-plane stress profile

(stress parallel to the interface) at the surface of TBC, which was obtained from the same simulation procedure as in Fig. 7.

Fig. 8 shows that within the 7.5 mm radius heated area a compressive stress exists. This decayed outside the heated zone and from ~8 mm outwards the stress became tensile and increased with distance from the central heated point. The same conclusion was also reported by Zhang et al. [7,30] regarding a sample under a 3-D thermal gradient. They found horizontal cracks in TBC in the area with the highest thermal gradient, instead of the region with the highest temperature. However, in our study, cracks were present at the highest temperature region, and not the highest stress region. Hence it is thought that the stress levels simulated in Fig. 8 are not sufficiently large to cause crack propagation. The microstructure of the flame treated ceramic coatings' fracture section indicated that sintering occurred in the TBC and was the dominant reason for the vertical cracks in TBC.

4.3. Residual stresses gradient

There were two components of residual stress obtained from the TBC using PLPS. One of them was macrostress, which was caused by the thermal mismatch between metallic substrate and YSZ TBC. As the heating time was very short, the influence of the TGO growth and creep of the metal substrate were neglected. Another component was so called microstress, which was induced by thermal mismatch between embedded alumina and YSZ ceramic coating matrix.

In substrate supported thermal barrier coatings, the stress gradient along through thickness direction was also induced by both macrostress and microstress. For the as

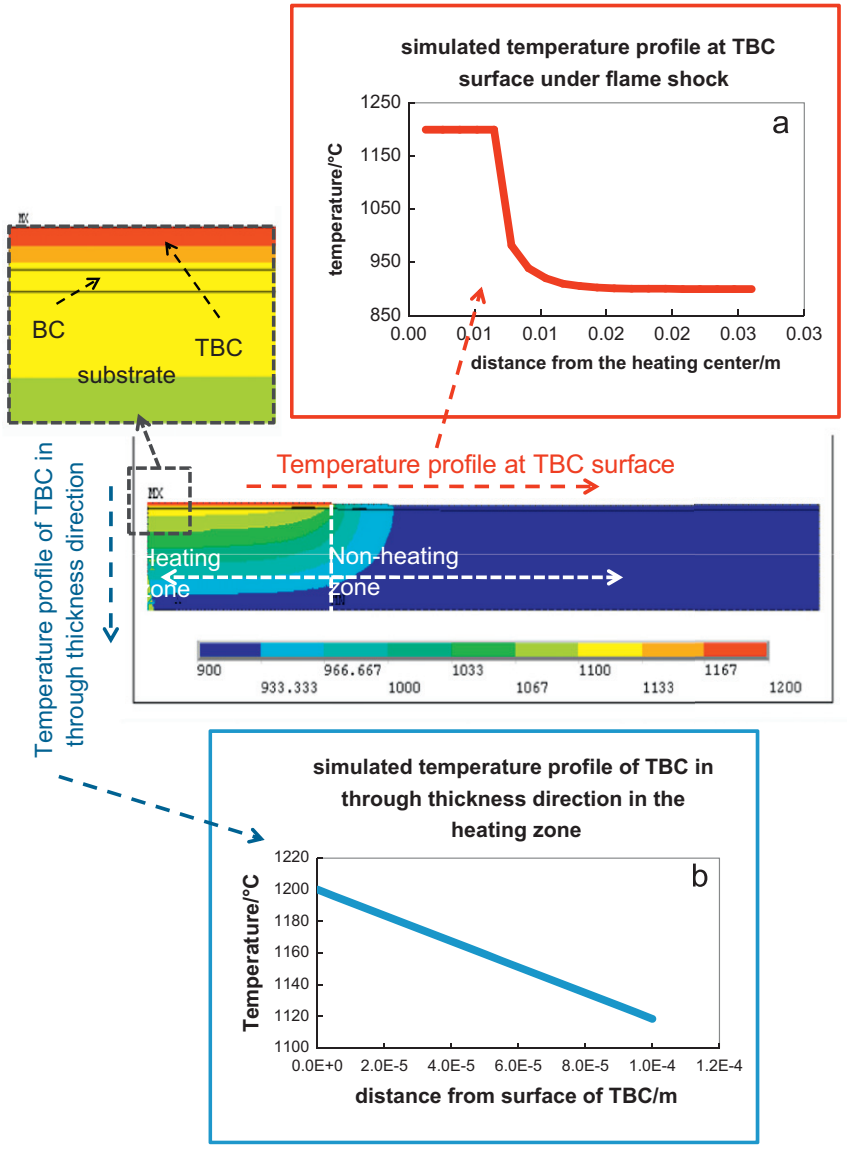

Fig. 7. Simulated temperature profile and its contour chart in the temperature keeping procedure under flame shock, (a) at the TBC surface, and (b) through the thickness direction. It should be noted that through the thickness direction, only the profile in the ceramic coating was illustrated.

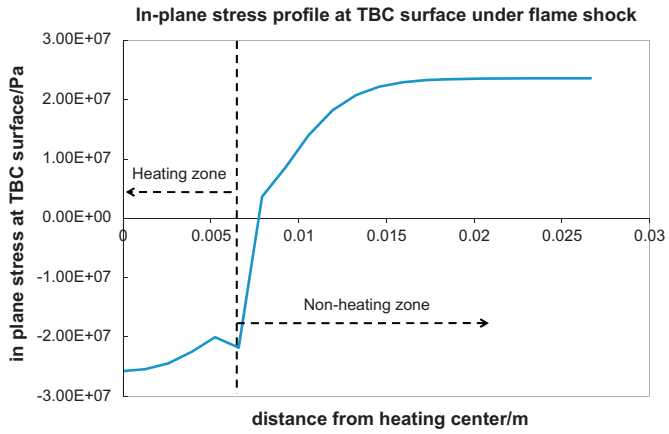

Fig. 8. In-plane stress profile at the surface of TBC in the temperature keeping procedure. Temperature at the TBC surface was 1200 °C, while at the substrate was 900 °C. The origin of the horizontal axis was the heating center. The radius heating area was 7.5 mm.

deposited EB-PVD coating, stress gradient was mainly contributed by the macrostress due to its columnar structure. However, after a certain period of heat treatment, sintering occurred in the ceramic coating, especially between columns. In this situation, the contribution of macrostress to the stress gradient along through thickness direction was limited, whereas microstress was the main reason to cause stress gradient. After the flame treatment, severe sintering of the ceramic coating was observed. Therefore, the stress gradient illustrated in Fig. 6 was considered to be mainly induced by microstress variation along through thickness direction.

It is widely accepted that microstress could be calculated by the following equation [31,32]:

$$\sigma_{mic} = \frac{\left(\alpha_{Al_2O_3} - \alpha_{YSZ}\right)\Delta T}{\frac{1+\nu_{YSZ}}{2E_{YSZ}} + \frac{1-2\nu_{Al_2O_3}}{E_{Al_2O_3}}} \quad (4)$$

where E is elastic modulus, α is thermal expansion coefficient, ν is Poisson′s ratio and ΔT is the temperature difference between the measurement and the deposition temperature of the coating [32,33]. From Eq. (4) it can be seen that for a given deposition temperature, microstress is mainly controlled by Young′s modulus of ceramic coating.

When the sample was exposed under flame, a temperature gradient along through thickness direction was attained, which was simulated in Section 4.1. This suggested that the sintering of the ceramic coating also varied along through thickness direction. At the surface of the coating, higher temperature was experienced during the flame treatment test. As a result, sintering induced densification in the surface part was also more severe than that in the underlying part of the coating. Although the sintering gradient could not be observed in the microstructure at cross section of the coating after the test, a stress gradient along through thickness direction was obtained using PLPS, which is shown in Fig. 6. Since the stress gradient in this situation was mainly controlled by microstress, the illustrated profile denoted Young′s modulus variation of the ceramic coating. Therefore, the temperature gradient induced gradient sintering of ceramic coating was proved.

Table 6
Mechanical parameters of materials at room temperature in TBC system.

	Young's modulus (GPa)	Poisson's ratio	Thermal expansion coefficient ($\times 10^{-6}$/°C)
Substrate	126	0.3	15
YSZ (as deposited)	48	0.1	9
YSZ (after sintering)	80	0.1	9
TGO/alumina	400	0.23	8

PLPS measurement was carried on the surface of the free standing TBC after the flame treatment with removing of the substrate. In this situation, since the substrate was removed, the macrostress was released, only microstress remained. The corresponding peak position was 14400.45, which indicates that the residual stress in this situation was 204 MPa. Using Eq. (4) and parameters in Table 6, it can be obtained that Young′s modulus at surface of flame treated TBC was 180 GPa.

At the mean time, the residual stress profile illustrated in Fig. 6 denoted the slope of the residual stress as a function of focus depth was around 0.005. According to the stress profile, Young′s modulus of the coating at the depth of 50 μm after the flame treatment was around 50 GPa, which was very close to Young′s modulus of as deposited ceramic coating.

The error bar of the stress profile in each depth was also illustrated in Fig. 6. It should be noticed that with the increasing of the focus depth, the error also increased. It was considered that with the increasing of focus depth, the obtained fluorescence signals weakened due to scattering and absorption [33]. At the mean time, the penetration depth of the fluorescence signal in EB-PVD ceramic coating is 30–40 μm. The data obtained from focus deeper than 40 μm might be the compact influence from the other part of the coating. Research in this area is still in proceeding.

5. Conclusions

Surface morphologies of TBC specimens exposed to different temperature regions during flame shock testing were studied. A finer crack network was observed in the hottest region of YSZ TBC after flame shock rather than in the region with the largest temperature gradient that suffered from the largest surface tensile stress.

The formation of the crack network was related to joining of main columns due to sintering of the ceramic coating. PLPS was employed to determine the residual stress gradient along through thickness direction. Compressive stresses decreased with the increasing of the focus

depth, indicating that more severe sintering of the ceramic coating occurred at the surface of the coating.

The coincidence of the areas with visible sintering and greatest stress, as measured by PLPS indicated that ceramic surface densification and accompanying volume shrinkage caused the formation of fine cracks in the flame heated area. This suggested that ceramic surface densification and volume shrinkage might be the dominant reason for early stage failure of TBC systems.

The gradient of the TBC′s Young′s modulus was also obtained from the microstress gradient along through thickness direction. This suggests that PLPS measurement along the through thickness direction is a potential non-destructive method for the determination of Young′s modulus of thermal barrier coatings, despite that the accuracy of the method is still in improvement.

References

[1] A.G. Evans, M.Y. He, J.W. Hutchinson, Mechanisms controlling the durability of thermal barrier coatings, Progress in Materials Science 46 (2001) 249–271.

[2] P.K. Wright, A. Evans, Mechanisms governing the performance of thermal barrier coatings, Current Opinion in Solid State and Materials Science 4 (1999) 255–265.

[3] D.R. Clarke, C.G. Levi, Materials design for the next generation thermal barrier coatings, Annual Review of Materials Research 33 (2003) 383–417.

[4] U. Schulz, B. Saruhan, K. Fritscher, C. Leyens, Review on advanced EB-PVD ceramic topcoats for TBC applications, International Journal of Applied Ceramic Technology 1 (2004) 302–315.

[5] A.F. Renteria, B. Saruhan, U. Schulz, H.J. Raetzer-Scheibe, J. Haug, A. Wiedemann, Effect of morphology on thermal conductivity of EB-PVD PYSZ TBCs, Surface and Coatings Technology 201 (2006) 2611–2620.

[6] R.G. Hutchinson, N.A. Fleck, A. Cocks, A sintering model for thermal barrier coatings, Acta Materialia 54 (2006) 1297–1306.

[7] C.X. Zhang, C.G. Zhou, H. Peng, S.K. Gong, H.B. Xu, Influence of thermal shock on insulation effect of nano-multilayer thermal barrier coatings, Surface and Coatings Technology 201 (2007) 6340–6344.

[8] H. Peng, H. Guo, C. Zhang, S. Gong, Numerical analysis of EB-PVD thermal barrier coatings under thermal-mechanical coupled environment, Materials Science Forum 546–549 (2007) 1795–1799.

[9] R. Vassen, F. Cernuschi, G. Rizzi, A. Scrivani, N. Markocsan, L. Ostergren, A. Kloosterman, R. Mevrel, J. Feist, J. Nicholls, Recent activities in the field of thermal barrier coatings include burner rig testing in the European Union, Advanced Engineering Materials 10 (2008) 907–921.

[10] A.T. Fry, J. Banks, J. Nunn, L.J. Brown, Comparison of the thermal cycling performance of thermal barrier coatings under isothermal and heat flux conditions, Material Science Forum 595–598 (2008) 77–85.

[11] H.B. Guo, H. Murakami, S. Kuroda, Effect of hollow spherical powder size distribution on porosity and segmentation cracks in thermal barrier coatings, Journal of the American Ceramic Society 89 (2006) 3797–3804.

[12] H. Guo, S. Kuroda, H. Murakami, Microstructures and properties of plasmasprayed segmented thermal barrier coatings, Journal of the American Ceramic Society 89 (2006) 1432–1439.

[13] M. Levit, I. Grimberg, B.Z. Weiss, Residual stresses in ceramic plasma-sprayed thermal barrier coatings: measurement and calculation, Materials Science and Engineering A 206 (1996) 30–38.

[14] P. Scardi, M. Leoni, L. Bertamini, Influence of phase stability on the residual stress in partially stabilized zirconia TBC produced by plasma spray, Surface and Coatings Technology 278 (1995) 106–112.

[15] J. Matejicek, S. Sampath, P.C. Brand, H.J. Prask, Quenching, thermal and residual stress in plasma sprayed deposits: NiCrAlY and YSZ coatings, Acta Materialia 47 (1999) 607–617.

[16] M.K. Hobbs, H. Reiter, Residual stresses in ZrO_2–8% Y_2O_3 plasma-sprayed thermal barrier coatings, Surface and Coatings Technology 34 (1988) 33–42.

[17] V. Teixeira, M. Andritschky, W. Fischer, H.P. Buchkremer, D. Stover, Analysis of residual stresses in thermal barrier coatings, Journal of Materials Processing Technology 92 (1999) 209–216.

[18] D. Greving, J. Shadley, E. Rybicki, D. Greving, J. Shadley, E. Rybicki, Effects of coating thickness and residual stresses on the bond strength of ASTM C633-79 thermal spray coating test specimens, Journal of Thermal Spray Technology 3 (1994) 371–378.

[19] M.M. Gentleman, D.R. Clarke, Concepts for luminescence sensing of thermal barrier coatings, Surface and Coatings Technology 188 (2004) 93–100.

[20] V.K. Tolpygo, D.R. Clarke, Alumina scale failure resulting from stress relaxation, Surface and Coatings Technology 120–121 (1999) 1–7.

[21] J.A. Nychka, D.R. Clarke, S. Sridharan, E. Jordan, M. Gell, M.J. Lance, C.J. Chunnilall, I.M. Smith, S. Saunders, R. Pillan, V. Sergo, A. Selcuk, A. Atkinson, K.S. Murphy, NDE assessment of TBCs: an interim report of a photo-stimulated luminescence 'round-robin' test, Surface and Coatings Technology 163 (2003) 87–94.

[22] L. Grabner, Spectroscopic technique for the measurement of residual stress in sintered Al_2O_3, Journal of Applied Physics 49 (1978) 580.

[23] X. Zhao, P. Xiao, Residual stresses in thermal barrier coatings measured by photoluminescence piezospectroscopy and indentation technique, Surface and Coatings Technology 201 (2006) 1124–1131.

[24] Q. Ma, D.R. Clarke, Stress measurement in single crystal and polycrystalline ceramics using their optical fluorescence, Journal of the American Ceramic Society 76 (1993) 1433–1440.

[25] J. He, D.R. Clarke, Determination of the Piezospectroscopic Coefficients for Chromium-Doped Sapphire, Journal of the American Ceramic Society 78 (1995) 1347–1353.

[26] Q. Ma, W. Pompe, J.D. French, D.R. Clarke, Residual stresses in Al_2O_3–ZrO_2 composites: a test of stochastic stress models, Acta Metallurgica et Materialia 42 (1994) 1673–1681.

[27] Y.C. Zhou, T. Hashida, Coupled effects of temperature gradient and oxidation on thermal stress in thermal barrier coating system, International Journal of Solids and Structures 38 (2001) 4235–4264.

[28] H.J. Ratzer-Scheibe, U. Schulz, The effects of heat treatment and gas atmosphere on the thermal conductivity of APS and EB-PVD PYSZ thermal barrier coatings, Surface and Coatings Technology 201 (2007) 7880–7888.

[29] X. Zhao, P. Xiao, Focus effect of photoluminescence piezospectroscopy and its influence on the stress measurement of thermally grown oxide in thermal barrier coatings, Scripta Materialia 57 (2007) 683–686.

[30] H.B. Xu, S.K. Gong, Y. Zhang, C.X. Zhang, Experimental and computational study on hot fatigue process of thermal barrier coatings by EB-PVD, Intermetallics 13 (2005) 315–322.

[31] X. Wang, P. Xiao, M. Schmidt, L. Li, Laser processing of yttria stabilised zirconia/alumina coatings on FeCr alloy substrates, Surface and Coatings Technology 187 (2004) 370–376.

[32] X. Wang, P. Xiao, Residual stresses and constrained sintering of YSZ/Al_2O_3 composite coatings, Acta Materialia 52 (2004) 2591–2603.

[33] S. Guo, R.I. Todd, Confocal fluorescence microscopy in alumina-based ceramics: where does the signal come from, Journal of the European Ceramic Society 30 (2010) 641–648.